Journal of Materials Chemistry C

ROYAL SOCIETY OF CHEMISTRY

PAPER

View Article Online
View Journal

Cite this: DOI: 10.1039/d5tc02366a

Efficient optical photoswitching of benzyloxy-substituted TCF-based D–π–A molecules

Kamila Lupinska, *[a] Kinga E. Szkaradek,[b] Kacper Parafiniuk,[a] Robert Góra,[b] Piotr Fita,[c] Yann Bretonnière,[d] Chantal Andraud[d] and Lech Sznitko *[a]

Received 19th June 2025,
Accepted 13th August 2025

DOI: 10.1039/d5tc02366a

rsc.li/materials-c

Molecules exhibiting photo-switching behavior are essential for the development of various photonic and optoelectronic devices. In this study, we report the synthesis of five novel donor–π–acceptor organic dyes, in which a stilbene moiety serves as a π-linker between the electron-donating and electron-withdrawing units. To address the challenge of developing photo-switchable molecules responsive to visible light, we performed fundamental optical characterization in both solution and solid state. The photoisomerization capability was confirmed for all compounds through real-time absorption measurements, enabling the calculation of $E \rightarrow Z$ isomerization kinetics. The presence of both isomeric forms was further validated by ^{1}H NMR spectroscopy. These experimental findings were supported by quantum chemical calculations, which identified the most stable conformers and accurately predicted their spectral properties. Moreover, pump–probe experiments demonstrated that irradiation with linearly polarized light efficiently triggers photo-induced birefringence in dye-doped polymer systems, with a notable "memory effect" observed for all studied compounds. Remarkably, the dyes are highly sensitive to light, and the birefringence saturation can be achieved at light intensities comparable to natural daylight, highlighting their broad potential application in optoelectronic devices.

Introduction

Recently, one of the main research focuses has been the design of photo-switchable molecules, due to their potential applications in various fields such as sensing, optoelectronics, and photon energy storage[1–3]. Molecular photoswitching can occur in a broad range of material systems, including liquid crystals,[4,5] metal–organic frameworks,[6,7] and organic dyes.[8,9] Organic compounds, in particular, offer significant advantages in comparison to other systems due to the relative ease of tuning their spectroscopic properties.[10] Additionally, they can be integrated into diverse media, such as liquid solutions or solid films,[11,12] while maintaining their photoresponsive behavior.

Among the various types of organic dyes, those featuring a donor–π–acceptor (D–π–A) architecture can exhibit multiple functionalities, depending on the specific molecular structures and substituents used during synthesis.[10,13] Their modular nature allows the design process to be compared to a "LEGO block" concept, where different properties can be tailored by simply varying the donor (D), π-bridge, or acceptor (A) components within a common synthetic framework. Moreover, the synthesis of these compounds is generally considered cost-effective, which represents a significant advantage for potential large-scale production and commercialization.

D–π–A molecules featuring vinyl π-linkers have attracted significant attention due to their ability to facilitate precise molecular-level control during photoisomerization.[14,15] Materials with reversible optical photoswitching,[16] responsiveness to visible light,[17] tunable optical properties, and controllable photoisomerization processes[18] are currently of great interest to researchers. These molecules are promising candidates for intelligent optical materials,[19,20] sensors,[21,22] and optical data storage,[23,24] as well as applications in optoelectronics[25] and super-resolution microscopy.[26] However, the alkene bond has the drawback of requiring UV light to induce the photoisomerization transition between its two forms, which limits its applicability.[25] To overcome this limitation, substituting D–π–A compounds with a strong electron-acceptor group, such as 2-dicyanomethylidene-3-cyano-4,5,5-trimethyl-2,5-dihydrofuran (tricyanofuran, TCF), can significantly red-shift the absorption spectrum, thereby enhancing the usability of these molecules within the visible range of the electromagnetic spectrum[10,27].

[a] Soft Matter Optics Group, Faculty of Chemistry, Wroclaw University of Science and Technology, Wybrzeze Wyspianskiego 27, 50-370 Wroclaw, Poland. E-mail: kamila.lupinska@pwr.edu.pl, lech.sznitko@pwr.edu.pl
[b] Institute of Advanced Materials, Faculty of Chemistry, Wroclaw University of Science and Technology, Wybrzeze Wyspianskiego 27, 50-370 Wrocław, Poland
[c] Institute of Experimental Physics, Faculty of Physics, University of Warsaw, 02-093 Warsaw, Pasteura 5, 02-093 Warsaw, Poland
[d] ENS de Lyon, CNRS UMR 5182, Laboratoire de Chimie, F69342, Lyon, France

In this work, we present a family of five different D–π–A structured compounds. Each molecule features a TCF acceptor group and a poly-benzyloxybenzyl donor group, connected *via* a vinylene linker to facilitate intramolecular charge transfer. It is important to note that the presented compounds share a structural similarity with dyes that have already been published[27]. Motivated by the interesting properties of those previously reported materials – such as solid-state emission and red-shifted luminescence toward the infrared region – our goal was to design and synthesize new compounds with improved solubility, expecting them to exhibit similar optical properties. To achieve this, we retained the same acceptor group but modified the donor part of the molecules. For the new family of dyes, we performed optical investigations like absorption and emission spectral measurements, both in solution and solid state, as well as photoluminescence lifetime and quantum yield estimations. We performed quantum chemical calculations to gain deeper insight into the photophysical properties of the investigated molecules, including the identification of their stable conformers and the nature of the ground-to-excited state transitions. Afterwards, we investigated $E \leftrightarrow Z$ photoisomerization through absorption spectroscopy and ^{1}H NMR measurements in DCM and $CDCl_3$, respectively. Finally, in a pump–probe experiment, we demonstrated that the synthesized molecules could function as efficient molecular switches for inducing optical birefringence (Δn) in dye-doped polymeric layers, even at very low pump intensities.

Results and discussion

Material synthesis

The synthesis of all five TCF-based derivatives was carried out using the Knoevenagel reaction, as illustrated in Fig. 1. This reaction was performed under microwave irradiation in anhydrous ethanol with a few drops of piperidine serving as a catalyst. The synthesis and characterization of the dyes, including ^{1}H NMR, $^{13}C\{^1H\}$ NMR, and high-resolution mass spectrometry (HRMS) analyses, which were performed on the powdered samples, are summarized in Fig. S1–S15.

Optical properties

The optical properties were measured in solution as well as in the solid state using powders directly obtained from the synthesis. Detailed experimental procedures can be found in the SI.

Optical properties in solutions

The absorption and emission spectra of compounds **1a–e** were measured in dilute tetrahydrofuran (THF) solutions. THF was chosen due to its intermediate polarity. The concentration was approximately 10^{-5} M for both absorption and photoluminescence (PL) measurements (see Fig. 2(a) and (b)). All compounds in this series exhibit broad absorption bands ranging from 320 nm to 550 nm, which is characteristic of D–π–A systems.[27] The optical properties of the dyes in THF solution are summarized in Table 1. As predicted, compound **1a** displays the most blue-shifted absorption maximum. This observation aligns with the general principle of this molecular systems: increasing the electron-donating strength of the donor segment typically leads to a red shift in the absorption spectrum.[10]

Di-benzyloxy compound **1b** shows a more red-shifted absorption band with respect to that of **1a**. Tri-benzyloxy **1d** shows an absorption maximum at 477 nm, while **1c** and **1e** absorption is blue-shifted. This may be caused due to steric hindrance, which reduces charge transfer between the donor and acceptor groups.[28] The molar absorption coefficient reaches approximately 20 000 M^{-1} cm^{-1} for **1b–e**, while for **1a**, it is around 28 000 M^{-1} cm^{-1}.

To obtain photoluminescence spectra, we excited solutions with wavelengths matching absorption maxima (see Fig. 2). Compounds **1a–e** were characterized by a large Stokes shift (from 2913 cm^{-1} obtained for **1d** to 5478 cm^{-1} for **1e**). However, such a significant value of the aforementioned shift is typical for molecules with this structural architecture. It is noteworthy that the spontaneous emission of the investigated compound family is placed mostly in the yellow region of light and in the yellow-orange light range for **1e** dye (see the CIE coordinates and diagram in Fig. 2(c) and (d)). The quantum yields of fluorescence (QYs) were calculated using a 10^{-1} M NaOH solution of fluorescein (QY = 79%) from ref. 29. The value of QYs for **1a–e** was relatively low, reaching 4.8% only for **1a**.

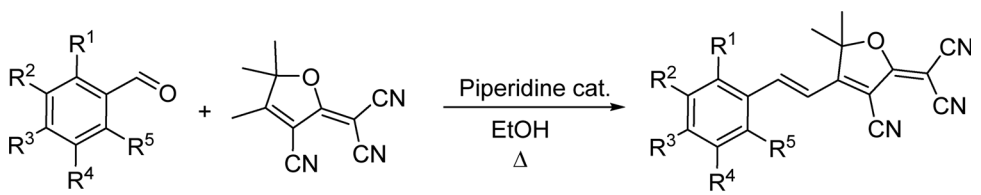

2a	$R^3 = OCH_2C_6H_5$	**1a** (75 %)
2b	$R^2 = R^3 = OCH_2C_6H_5$	**1b** (63 %)
2c	$R^1 = R^2 = R^3 = OCH_2C_6H_5$	**1c** (35 %)
2d	$R^1 = R^3 = R^5 = OCH_2C_6H_5$	**1d** (85 %)
2e	$R^2 = R^3 = R^4 = OCH_2C_6H_5$	**1e** (57 %)

Fig. 1 Synthesis scheme of molecules **1a–e**.

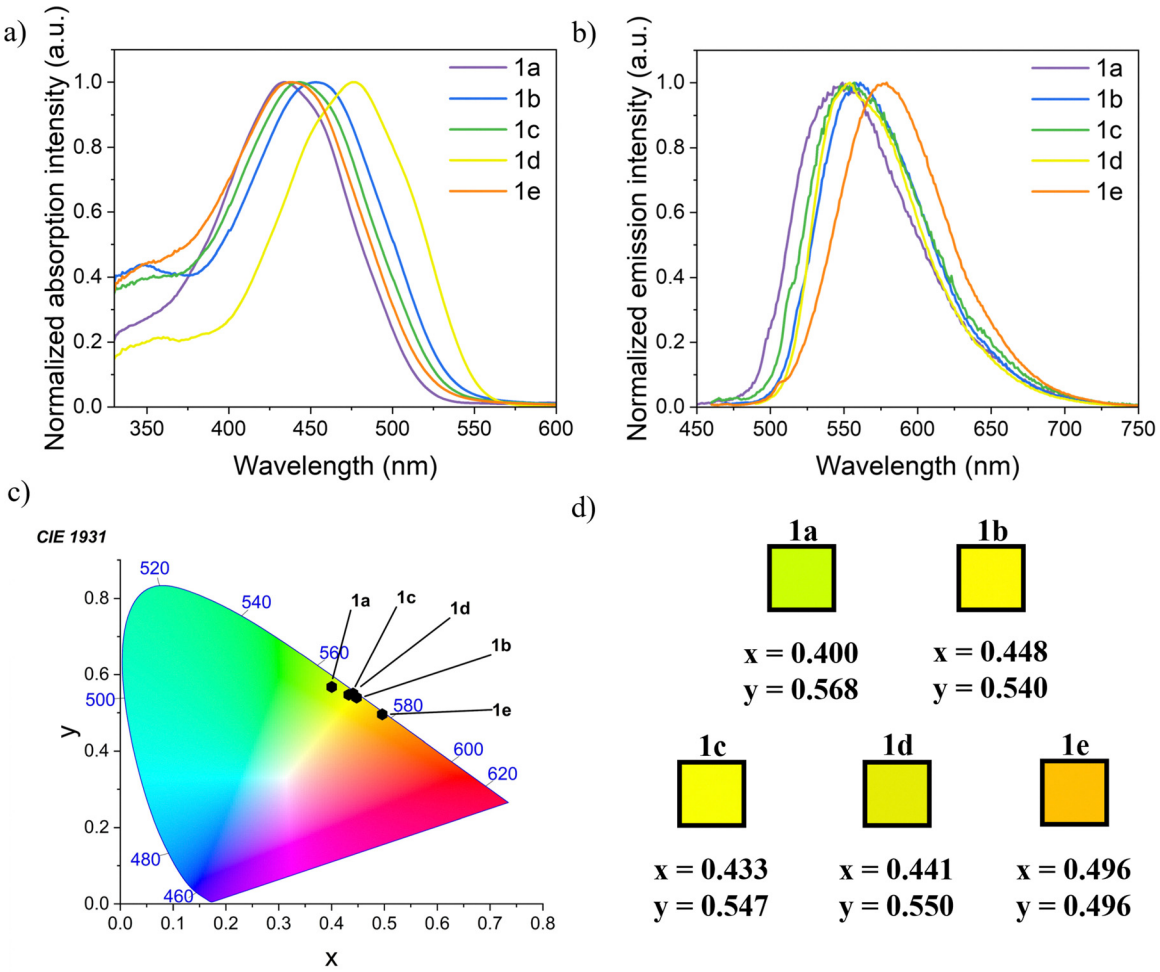

Fig. 2 (a) Absorption and (b) emission spectra of **1a–e** in $\sim 10^{-5}$ THF solutions. (c) CIE 1931 graph calculated for the emission spectra (d) with the *x* and *y* coordinates placed under the squares filled with the corresponding colors. Emission was recorded at an excitation wavelength equal to the maximum of the absorption spectra of each compound.

Details about measurements are presented in the Materials and methods section in the SI.

Optical properties in the solid state

In all cases, the fluorescence obtained for solids shifts towards the red region of light (Fig. 3(a)), which might be important from an application point of view.[30,31]

The fluorescence measurements were performed directly on powders (see details in the SI). The emission maxima of **1a–e** are located between 587 nm (**1c**) and 641 nm (**1e**), which corresponds to the orange-red region (see the CIE 1931 coordinates in Fig. 3(b) and (c)). The most significant shift was observed for **1e**, with a value of 202 nm (7180 cm^{-1}). **1b**, which differs in one –OBn group from **1e** at the *meta* position, shows a relatively high value of the solid–liquid shift as well, namely, 168 nm (5974 cm^{-1}). On the other hand, **1c** shows the lower value of Stokes shift – 144 nm (5546 cm^{-1}). The photoluminescence quantum yields for solids were determined using a direct method utilizing an integrated sphere (see Methods details in the SI). The values of the QYs in solids compared to those estimated in solutions were significantly higher. Dyes **1a** and **1d** achieve a similar quantum yield of $\sim$8%. The most noteworthy results are QYs up to 22% for **1b** and 14% for **1d**. Additionally, we measured the lifetimes (τ) of the PL for the powders (see Fig. S16 and S17). Photoluminescence lifetimes for **1a–d** were estimated using a double exponential fit, where amplitudes are expressed as the percentage of each time constant contribution. The longest exponential decay was measured for **1b**, for which values of decay times of 4.9 ns (75%) and 2.1 ns (25%) were determined. The rest of the PL lifetimes for the dyes oscillated around 1–2 ns. Additionally, we calculated the radiative and non-radiative rate constants for the studied compounds in the solid state. Since all of the presented photoluminescence decay curves were best fitted with a bi-exponential model, we decided to utilise the weighted-average photoluminescence lifetime. The rate constants were calculated using a simple approach, as presented below:[32]

$$k_r = \frac{\Phi_{ss}}{\tau_{av}} \quad (1)$$

Table 1 Optical properties of **1a–e** in solution and solid state

	Solution				Solid state		
Dye	λ_{abs} (nm)/ε^a (M^{-1} cm^{-1})	$\lambda_{emi}{}^a$ (nm)	$\Delta\lambda$ (nm)/(cm^{-1})	Φ^{ab} (%)	λ_{emi} (nm)	Φ^c (%)	τ^d (ns)
1a	434/27 942	548	114/4794	4.8	599	8.3	τ_1 = 0.40 (50%) τ_2 = 1.20 (50%)
1b	453/22 250	560	107/4218	<1	621	22	τ_1 = 2.10 (25%) τ_2 = 4.90 (75%)
1c	443/21841	556	113/4587	<1	587	8.8	τ_1 = 0.42 (86%) τ_2 = 0.89 (14%)
1d	477/25 410	554	77/2913	<1	637	14	τ_1 = 0.87 (46%) τ_2 = 1.80 (54%)
1e	439/21 417	578	139/5478	<1	641	n.d.	n.d.

[a] THF solution. [b] Using 10^{-1} M NaOH solution of fluorescein as a reference (QY = 79%).[29] [c] Absolute quantum yield measured using a calibrated integrative sphere in direct excitation. [d] Values presented in parentheses are relative amplitudes of PL decay fitted with the two-exponential model.

$$k_{nr} = \frac{1 - \Phi_{ss}}{\tau_{av}} \quad (2)$$

where k_r is the radiative rate constant, k_{nr} is the non-radiative rate constant, Φss is the fluorescence quantum yield estimated for solid-state emission, and τ_{av} is the weighted-average photoluminescence lifetime. It is important to note that for all dyes, we clearly observe $k_{nr} > k_r$, indicating that non-radiative processes are dominant. However, for compound **1b**, which exhibits the highest values of τ_{av} and Φ_{ss}, the ratio between k_r and k_{nr} is the smallest, suggesting a higher fluorescence efficiency compared to the rest of the dyes. For the values of both rate constants and the averaged photoluminescence lifetimes, please refer to Table 2.

Quantum chemical calculations

The representative sample of the energetically lowest conformers of compounds **1a–e** has been selected based on metadynamic simulations at the GFN2-xTB level.[33] Among several exchange–correlation functionals tested (*cf.* Table S2), we chose PBE0, which shows good agreement with the experimental spectra. The equilibrium molecular structures were determined using the PBE0-D3BJ functional with dispersion correction and assuming an aug-ccpVDZ basis set and a PCM implicit solvent model, as implemented in the GAUSSIAN 16 package.[34] Vertical excitation spectra were then calculated using the TD-DFT method (*cf.* Table 3). We performed these calculations using a PCM model, focusing on the results obtained for THF, primarily because the basic spectroscopic properties were measured in this solvent.

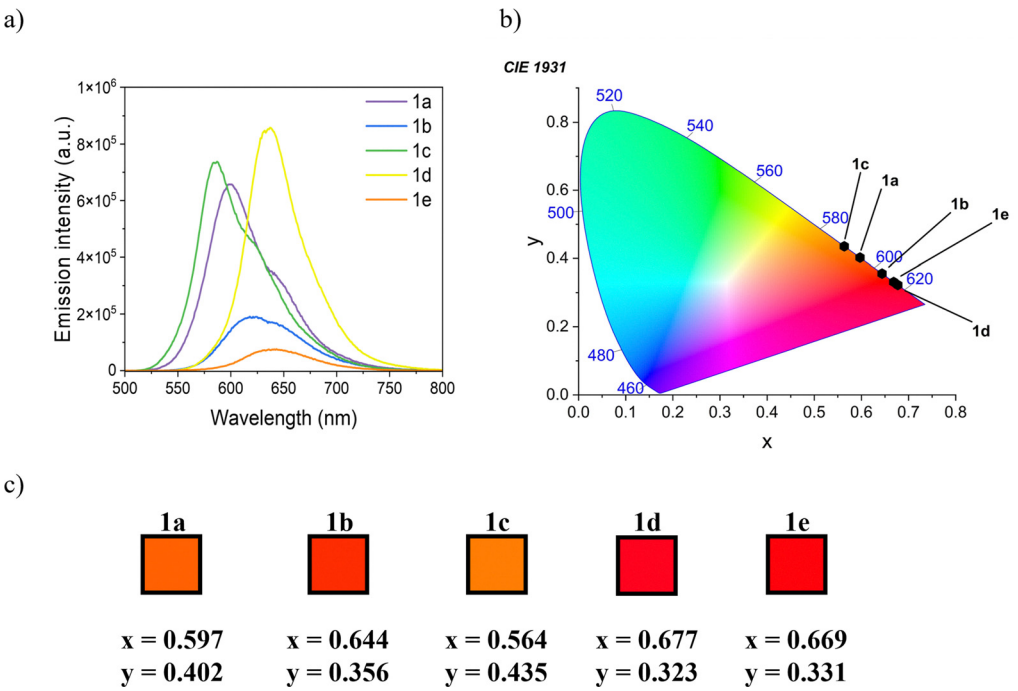

Fig. 3 (a) Emission spectra of compounds **1a–e** in the solid state; (b) CIE 1931 graph calculated for the emission spectra (c) with the *x* and *y* coordinates placed under the squares filled with the corresponding colors. Emission was recorded at an excitation wavelength equal to the maximum of the absorption spectra of each compound.

Table 2 Average photoluminescence lifetime (τ_{av}) and radiative (k_r) and non-radiative (k_{nr}) rate constants for the studied compounds in the solid state

Dye	τ_{av} (ns)	$k_r \times 10^8$ (s^{-1})	$k_{nr} \times 10^8$ (s^{-1})
1a	0.80	1.04	11.5
1b	4.20	0.52	1.86
1c	0.49	1.80	18.6
1d	1.37	1.02	6.23
1e	n.d.	n.d.	n.d.

Considering that the studied dyes have several plausible rotamers, we performed a detailed conformational search for the simplest molecule **1a** and focused on the most stable rotamers of the remaining compounds. Among the optimized structures of **1a**, we found ***E*** and ***Z*** isomers of the ethylenic bridge (–HC═CH–) and bent- (**b**) and axial-like (**a**) conformers of the methoxy bridge (–O–CH_2–) in the –OBn group (*cf.* SI). The latter differ in the mutual orientation of phenyl rings (the dihedral angle of the R–O–CH_2–R is either ∼180° in the '**a**' form and ∼75° in the '**b**' form). The ***E*** isomers are found in two nearly isoenergetic conformations, which differ in the orientation of the ethylenic bridge.

According to our calculations in the ground state, only the ***E′*** and ***E″*** isomers with the axial or bent orientation of –OBn groups are likely to be present in the solution as the located ***Z*** isomers that are over 20 kJ mol^{-1} are less stable (see the SI for details). Thus, in the case of compounds **1b–e**, we focused on the ***E′*****b** and ***E″*****b** isomers. The most relevant results are shown in Table 3, with more data reported in the SI.

Considering the size of the studied compounds, we chose **1a** for further studies of the photoisomerization mechanism. Fig. 4 shows a schematic representation of the most likely *E*–*Z* photoisomerization pathway of the ***E′*****b** isomer of **1a**. To obtain more reliable relative energies, the XMS-CASPT2/cc-pVDZ energies were calculated using the BAGEL package[35] at the geometries obtained using the PBE0-D3BJ/def2-SVP/CPCM(THF) approach implemented in the ORCA 6.0.1 package.[36] The ***E′*****b** isomer, after photoexcitation to the S_1 $^1\pi\pi^*$ state having a significant charge-transfer (CT) characteristic (from phenyl to TCF), undergoes structural relaxation (mainly bond-length alteration) to the S_1 (*E*) state minimum with a similar geometry. Further relaxation leads to an intermediate structure with the ethylenic –HC═CH– bridge rotated by 90°, which is close to the conical intersection with the ground state (the S_1–S_0 energy gap is only 0.2 eV at the PBE0-D3BJ/def2-SVP/PCM(THF) level) and then to the ***Z′*****b** isomer. To further confirm this mechanism, we performed a simulation of the emission band of the latter using the Adiabatic Hessian approach implemented in the excited state dynamics[37] subroutine of an ORCA 6.0.1 package,[36] which agrees well with the experimental data (Fig. S18). The calculated fluorescence rate is 5.908×10^8 s^{-1} (τ = 1.69 ns). The character of the S_1 state is essentially a HOMO–LUMO transition (see Fig. 4), and it remains virtually unchanged throughout the *E*–*Z* photoisomerization process, although for the rotated S1 structure, it becomes a dark state. The low wavelength shoulder of the

Table 3 Relative S_0 energies (ΔE_{SO}), vertical excitation energies (E_{exc}) of the bright S_1 state, the corresponding wavelengths and oscillator strengths (f_{osc}) of the selected **1a–e** rotamers (depending on the orientation of phenyl rings in the donor part of the dye) calculated using the PBE0-D3BJ/aug-cc-pVDZ/PCM(THF) method at the respective ground state local minima. The experimental absorption spectra are also shown for reference

			λ_{abs} (nm)		
Compound	ΔE_{S0} (kJ mol^{-1})	E_{exc} (eV)	Calc.	Exp.	*F*osc
1a (***E′*****b**)	0	2.783	445	434	1.63
1a (***E″*****b**)	2.57	2.733	454		1.39
1a (***E′*****a**)	3.39	2.776	447		1.70
1a (***E″*****a**)	5.57	2.729	454		1.48
1b (***E′*****b**)	0	2.613	474	453	1.52
1b (***E″*****b**)	2.16	2.579	481		1.24
1c (***E′*****b**)	0	2.722	455	443	1.52
1c (***E″*****b**)	2.33	2.669	464		1.24
1d (***E′*****b**)	0	2.704	458	477	1.63
1d (***E″*****b**)	2.03	2.662	466		1.33
1e (***E′*****b**)	0	2.538	488	439	1.15
1e (***E″*****b**)	0.28	2.510	494		1.07

experimental absorption band may be due to the S_2 $^1\pi\pi^*$ locally excited (LE) state, localized mostly at the TCF fragment, which, according to PBE0-D3BJ/aug-cc-pVDZ/PCM(THF) calculations, lies at 3.55 eV (349 nm) for **1a**. However, the computed oscillator strengths are usually substantially smaller than that for the bright S_1 state (0.02–0.06) – only for the **1b** dye, the computed relative oscillator strengths for $S_0 \rightarrow S_1$ and $S_0 \rightarrow S_2$ transitions correspond to the experimental relative intensities, and for the ***E′*****b** isomer, they amount to 1.22 and 0.30, respectively. The energy differences between rotamers are low enough (see Table 3) that molecules at room temperature can freely undergo rotameric transitions. Only the presence of isomeric structural changes (*E* to *Z* and *Z* to *E*) can be identified in the performed spectroscopic experiments. Thus, in the next sections of the article, we decided to streamline the nomenclature, and we simply categorized all conformers as *E* and *Z*, depending only on the rotation around the ethylene bridge (–HC═CH–), without distinguishing between rotameric states.

Photochromism

The photochromic reaction based on photoisomerization between stable conformers of the studied dyes, predicted in quantum chemical calculations, was further investigated experimentally by UV-VIS absorption measurements and NMR spectroscopy. Finally, we also checked if cyclic photoisomerization can lead to molecular photo-orientation and, thus, induce optical birefringence.

Real-time absorption measurements

The photoisomerization process can be monitored by measuring the intensity of the absorption band of the *E* and *Z* isomers (see details in the SI). In our case, the reaction was carried out in dichloromethane (DCM) solution with a concentration of $C = \sim 10^{-5}$ M. DCM was chosen as the solvent due to its medium polarity and lack of light absorption in the UV region, where the *Z*-isomers of the dyes are expected to absorb.

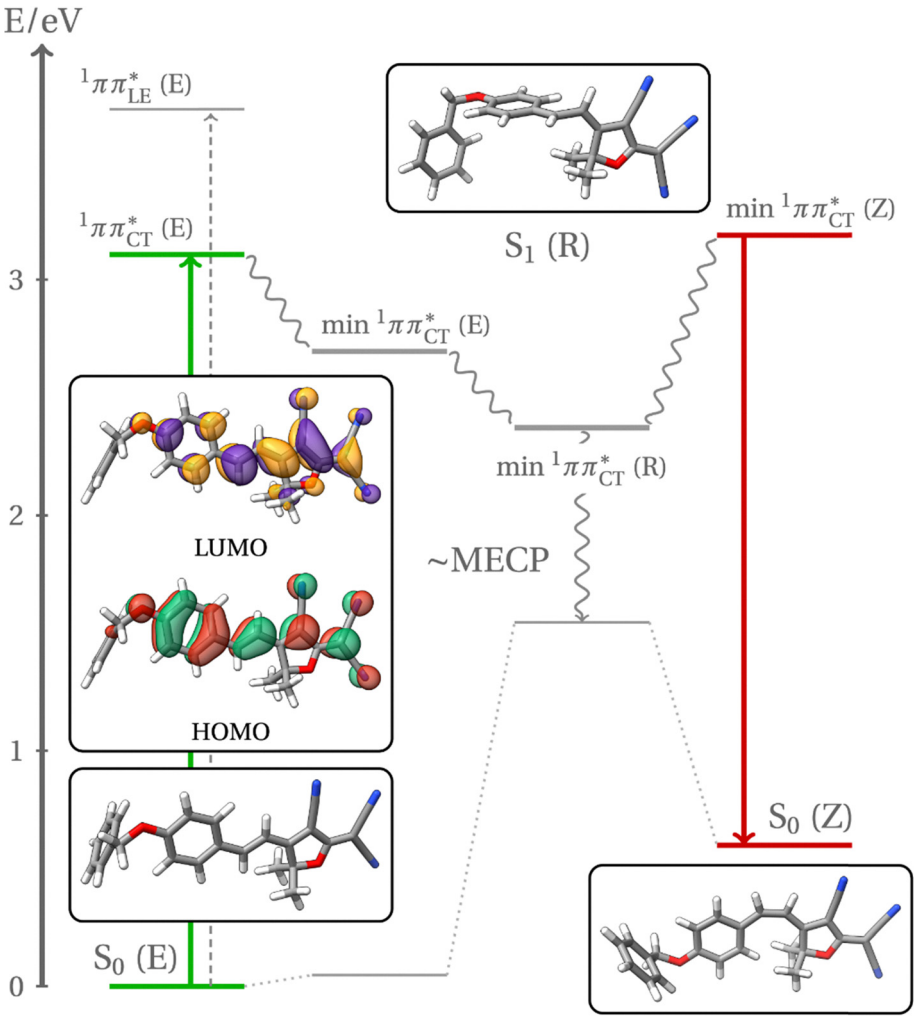

Fig. 4 A schematic representation of the most likely *E*–*Z* photoisomerization pathway of dye **1a**. The relative XMS-CASPT2(6,6)/cc-pVDZ energies were calculated at the geometries obtained using a PBE0-D3BJ/def2-SVP/PCM(THF) method. The rotated $^1\pi\pi^*$ (*R*) intermediate is close to the minimum-energy crossing point (MECP) with the ground state.

Although the quantum chemical calculations were performed using THF as the solvent model, the polarity of DCM is comparable to that of THF. Therefore, we considered it reasonable to compare the experimental and theoretical results, assuming only a small margin of error between the two solvents. The absorption of *E* isomers is located at around ~430–470 nm, while *Z* isomers can absorb the light near ~370 nm. By changing the wavelength of the light irradiation, we can control the relative concentration of both conformers, obtaining the typical photo-switching behavior. Thus, we used the 455 nm light irradiation to force transformation for all of the studied compounds. This transition can be observed in absorption spectra as the *E* band decreases with the increase of the *Z* band (see Fig. 5(a) and (b) for the representative compound **1a**). When we obtained the photostationary state for the $E \rightarrow Z$ photoisomerization, we used 365 nm light to obtain a reverse transition. The well-defined isosbestic points clearly show that the isomerization reaction is carried out only between the dyes' isomers.

The photoisomerization degree (Table 4) for the $E \rightarrow Z$ transition was obtained using eqn (3):

$$S = \frac{A_0 - A_\infty}{A_0} \times 100\%, \quad (3)$$

where A_0 is the absorbance just before the irradiation and A_∞ is the absorbance in the photostationary state at the maximum of the *E* band. The degree of photoisomerization varies between 31 and 50% for different compounds and is shown in Table 4. The kinetics data (Fig. 6(c)) present the determination of the *k* for **1a**, and Fig. S19 shows kinetics data for **1b–1e**. However, it is worth noting that, based on ^{1}H NMR measurements, the irradiation of the samples at 455 nm, which is used to determine the *S*(%), results in a simultaneous decrease in the signals corresponding to the *E* isomers and an increase in the signals associated with the *Z* isomers. Nevertheless, the whole process can be obtained by the calculation of the slope coefficient in the linear function plotted as a logarithmic

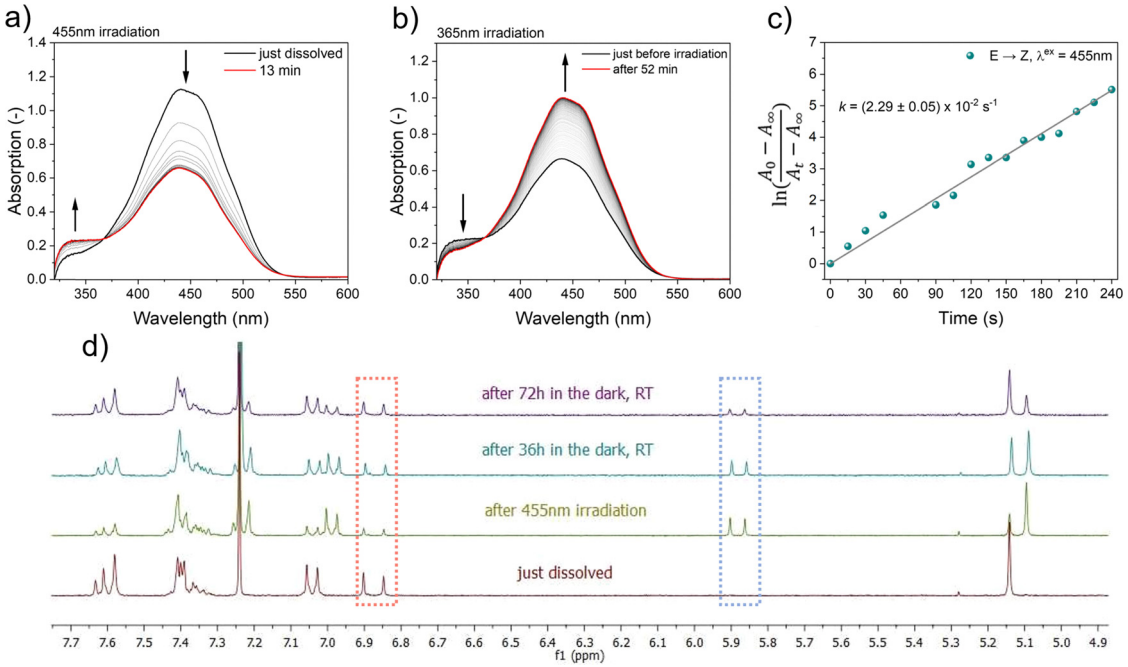

Fig. 5 The electronic absorption spectra of compound **1a** over the period of irradiation at (a) 455 nm and (b) 365 nm, (c) the dependence of $\ln\left(\frac{A_0 - A_\infty}{A_t - A_\infty}\right)$ as a function of the time and (d) the changes in the ^{1}H NMR spectra, with regions characteristic of the *E* and *Z* transitions highlighted by dotted red and blue rectangles, respectively.

Table 4 The kinetic rate constant (k) of the $E \rightarrow Z$ isomerization under 455 nm irradiation was determined for the studied compounds in DCM solution ($C \approx 10^{-5}$ M) at room temperature. The values are expressed in s^{-1} and the corresponding isomerization times are expressed in seconds. R^2 represents the goodness of fit of the linear regression, and S denotes the photoisomerization degree (and it was calculated for the maximum absorption wavelength for the *E* isomer)

	$E \rightarrow Z$			
Compound	k (s^{-1})	k (s)	R^2	S (%)
1a	$(2.29 \pm 0.05) \times 10^{-2}$	44 ± 1	0.9947	42
1b	$(3.04 \pm 0.07) \times 10^{-2}$	33 ± 1	0.9954	50
1c	$(3.43 \pm 0.14) \times 10^{-2}$	29 ± 2	0.9861	31
1d	$(3.13 \pm 0.05) \times 10^{-2}$	32 ± 1	0.9963	n.d.
1e	$(3.37 \pm 0.11) \times 10^{-2}$	30 ± 1	0.9898	41

dependence of the time:[38]

$$f(t) = \ln\left(\frac{A_0 - A_\infty}{A_t - A_\infty}\right) = kt, \quad (4)$$

where $A(t)$ is the value of the absorbance as a function of time and k is the kinetic constant, shown in Table 4. It is clear to see that the slowest transition of the *E*–*Z* photoreaction is observed for the **1a** molecule, which can be determined by the most favorable molecular arrangement obtained in the *E* form of the isomer. Note that **1c** and **1e** have the fastest kinetic reaction with respect to the other dyes.

The structural changes of all compounds were also studied by ^{1}H NMR analysis (the details of the experiment can be found in the Materials and methods section of the SI). For all samples (see Fig. 5(d) and Fig. S20–S23), irradiation at 455 nm resulted in a decrease in the doublet characteristic of the CHs of the *trans* double bond (*i.e.*, doublet at around 6.85 ppm, $J \sim 16.4$ Hz, marked with the red rectangle in Fig. 5(d)) and the appearance of the new doublet characteristic of the CHs of the *Z* double bond (*i.e.*, doublet at 5.8–5.9 ppm, J – 12.1 Hz). For the exact positions of the *E* and *Z* isomer doublets and their relative integration values over time, see Table S5. Please note that **1d** was the only dye to exhibit the presence of *Z* isomers immediately after dissolution, as observed in the ^{1}H NMR spectra.

Photoinduced birefringence

The photoisomerization process can lead to the development of optical birefringence in the sample. Typically, the optical anisotropy for azo-dyes is obtained by molecular ordering through the Weigert effect.[39] Such optically induced birefringence can be used to construct optical valves or to store optical data. As our previous experiments have shown, photoisomerization can be obtained for all of the molecules described here. Thus, we decided to investigate if they can also generate optical anisotropy. The experiment was carried out in the so-called pump–probe optical setup for dye-doped polymeric samples inserted between two crossed polarizers, where the DPSS diode laser of wavelength 473 nm was used to induce optical birefringence while the He–Ne laser was probing the induced Δn over time.

The details of the experiment and materials preparation are provided in the SI. Afterwards, we can calculate the value of

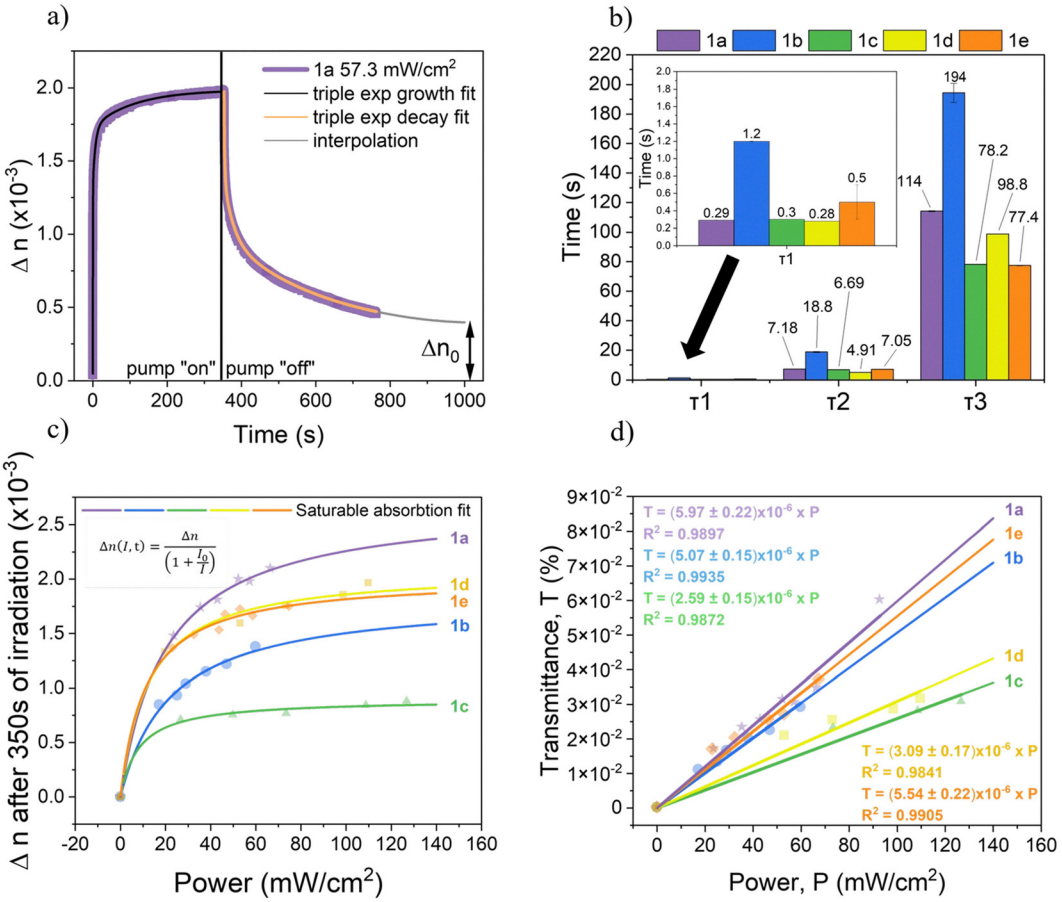

Fig. 6 (a) Impact of the external light on the changes in optical birefringence for **1a**, (b) time constant for the growth curve measured for all of the studied compounds, (c) saturable refractive index fit, and (d) linear dependence of changes in transmittance (ΔT) as a function of pump intensity (I).

photoinduced birefringence measured in a crossed-polarized system, namely, Δn (I_{pump}, t), using the below equation:[40]

$$\Delta n(I_{pump}, t) = \frac{\lambda_{probe}}{\pi d} \arcsin\left(\sqrt{\Delta T(I_{pump}, t)}\right), \quad (5)$$

where λ_{prob} is the wavelength of the probe laser, d is the thickness of the sample, and ΔT (I_{pump}, t) is the sample transmittance. In all of the cases, the measurements were conducted on the polymeric layers made of the dye-doped poly(methyl methacrylate) (PMMA) polymer with a concentration of 2%. Nevertheless, for the whole family, we noticed a typical exponential growth of intensity, which can correspond to the optical birefringence caused by the multiple changes in the molecular conformations.[41] On the other hand, when the laser pump is off, we cannot obtain the return of the material to the initial value of Δn (see Fig. 6(a) and Fig. S24), confirming the long-time thermal relaxation for the studied materials.

Both growth and decay curves have shown complex dynamics and could only be fitted by the triple exponential functions with considerable accuracy. All time constant values were determined for the used power of the laser pump ($\sim$60.5 $\pm$ 6.9 mW cm^{-2}) (see eqn (6) for the growth and eqn (7) for the decay, and Fig. 6(a)). The values of the calculated time constants are shown in Table S6,

$$\Delta n^{gr} = \Delta n_1^{gr} \cdot \left(1 - \exp\left(-\frac{t - t_0}{\tau_1^{gr}}\right)\right) + \Delta n_2^{gr} \cdot \left(1 - \exp\left(-\frac{t - t_0}{\tau_2^{gr}}\right)\right) + \Delta n_3^{gr} \cdot \left(1 - \exp\left(-\frac{t - t_0}{\tau_3^{gr}}\right)\right) \quad (6)$$

$$\Delta n^{dec} = \Delta n_0 + \Delta n_1^{dec} \cdot \left(\exp\left(-\frac{t - t_0}{\tau_1^{dec}}\right)\right) + \Delta n_2^{dec} \cdot \left(\exp\left(-\frac{t - t_0}{\tau_2^{dec}}\right)\right) + \Delta n_3^{dec} \cdot \left(\exp\left(-\frac{t - t_0}{\tau_3^{dec}}\right)\right) \quad (7)$$

where Δn_{1-3}^{gr} and Δn_{1-3}^{dec} are amplitudes of growth and decay curves, respectively, while τ_{1-3}^{gr} and τ_{1-3}^{dec} are the corresponding time constants, t_0 is the time when laser light irradiation was turned on or off, and Δn^{dec} is a constant birefringence observed after decay. It is worth adding that in all cases, we observed the memory effect, and once the placed sample was irradiated by the pumping laser, the birefringence never returned to the 0 value. Exemplary Δn dynamics for the **1a** molecule with fitting functions is shown in Fig. 6(a).

Table 5 The values of the Δn, I_0, Δn_0, and ξ for **1a–e**

Compound	Δn	SD[a] (Δn)	I_0 (mW cm^{-2})	SD[a] (I_0)	R^2	Δn_0[b]	ξ[c] (%)
1a	2.7×10^{-3}	8.1×10^{-5}	20	2	0.9986	3.97×10^{-4}	14.65
1b	1.8×10^{-3}	1.0×10^{-4}	22	4	0.9937	2.58×10^{-4}	14.02
1c	9.0×10^{-4}	3.4×10^{-5}	8	3	0.9914	2.22×10^{-4}	24.69
1d	2.1×10^{-3}	8.5×10^{-5}	12	3	0.9902	1.72×10^{-4}	8.23
1e	2.0×10^{-3}	8.0×10^{-5}	11	3	0.9939	4.44×10^{-4}	21.98

[a] SD(−) is the standard deviation of value. [b] The Δn_0 was estimated from the extrapolated triple exponential decay fit over 1000 seconds to obtain a plateau. [c] ξ represents the percentage share of Δn_0 in Δn.

Growth time constants are shown in Fig. 6(b). It is clearly seen that in the case of the growth curve, the shortest time constant (τ_1^{gr}) presents the highest amplitude, based on calculated Δn, which was estimated using eqn (6) (see Table S6). On the other hand, the τ_2^{gr} and τ_3^{gr} present the lowest amplitude, with a value between 4 and 18 s for τ_2^{gr} and with a range of 77 s to 194 s for τ_3^{gr}. When we consider the decay curve for all of the studied compounds, we see a relatively equal distribution for each of the time constants except for **1b** and **1d**, where the τ_1^{gr} presents a visibly higher contribution than τ_2^{gr} and τ_3^{gr} (Table S6).

Due to the observed saturation effect in photoinduced birefringence (see Fig. 6(c)) at low power pump intensity, which is due to the saturation of *E* isomer absorption, we propose to fit obtained data with the following expression (see the derivation in the SI):

$$\Delta n(I) = \frac{\Delta n}{\left(1 + \frac{I_0}{I}\right)}, \quad (8)$$

where $\Delta n(I)$ is the maximal birefringence for intensity I, Δn is the maximal birefringence for the given system when $I \rightarrow \infty$, and I_0 is the saturation intensity. Note that the I_0 values measured for all of the dyes are exceptionally small. For instance, compound **1c** achieves its saturation level at the pump intensity as low as 8 mW cm^{-2}. On the other hand, **1b** presents $I_0 \sim 22$ mW cm^{-2} (see Table 5). Moreover, the most striking fact is that available birefringence values for the measured samples are on the order of 10^{-4}–10^{-3}, which is a significant value with respect to other systems utilizing small, isomerizable molecules for the generation of optical birefringence.[42–44]

Fast saturation and strong nonlinear character can be seen as disadvantages in various optical modulators. Luckily, for the mentioned application, typically, the value of interest is the transmittance or transmitted light intensity. In Fig. 6(d), we plot the transmittance ΔT obtained using crossed polarizers *vs.* pumping beam intensity.

Discussion

The analysis of the optical properties of the studied compounds, both in solution and in the solid state, shows that only compound **1a** exhibits a photoluminescence quantum yield above 1% in solution. Please note that compound **1d** exhibited the lowest Stokes shift among the studied dyes (in solution). This may be caused by the bonding effect of the –OBn groups on the carbon–carbon double bond, which could disturb the planarity of the entire system. As a result, this may interfere with the charge transfer between donor and acceptor groups, disrupt electron delocalization, and thus blue-shift the emission spectrum. (Please refer to Table S7 for the corresponding calculations.)

Additionally, the photosensitivity of the materials was evaluated through real-time monitoring of their absorption spectra under irradiation at two different wavelengths (455 nm and 365 nm). The results demonstrated full reversibility of isomerization processes in liquid environments, with the kinetics of the $E \rightarrow Z$ transformations indicating a rapid response that can be triggered even under daylight conditions. As previously mentioned, the rate of isomerization depends on the molecular structure, specifically the number and position of –OBn substituents. Compounds **1c** and **1e** exhibited the fastest $E \rightarrow Z$ transitions, whereas **1a** showed the slowest response.

Structural changes between the isomeric forms were confirmed by ^{1}H NMR spectroscopy. Note that the ^{1}H NMR measurements were performed in deuterated chloroform – $CDCl_3$ (unlike in the case of calculation and real-time absorption measurements). Please note that *Z*–*E* photoisomerization can occur in different solvents for all dyes, indicating their versatility and making them ideal for photoswitching applications. Notably, thermal relaxation back to the initial *E* form was observed only for compounds **1d** and **1e**, as confirmed by the reappearance of characteristic signals in the ^{1}H NMR spectra (considering the given time of 72 h). Please note that the relative integration of the respective *E*/*Z* doublets presented in Table S5 clearly shows a decrease in the integration of the doublet corresponding to the *Z*-isomer over time. This observation indicates that thermal relaxation does occur for these dyes, although it proceeds at a significantly slow rate. In contrast, for compounds **1a**, **1b**, and **1c**, the doublet corresponding to the *Z* isomer remained detectable even after 72 hours in the dark, indicating a significantly slower thermal back-isomerization process. This prolonged stability of the *Z* isomer suggests that such compounds, particularly **1a–1c**, may hold potential for optical data storage applications, where long thermal relaxation times are considered highly advantageous.[45]

The typical nonlinear refractive index parameter (n_2) could not be accurately determined, as the system appears to reach a saturation regime, where the birefringence response no longer follows a linear dependence on pump intensity. Nevertheless, for all of the studied compounds, we estimated the relevant parameters using eqn (8) (see eqn (S11)), which accounts for saturable absorption. This approach yielded excellent fits, with

R^2 values exceeding > 0.99 for all samples. Importantly, based on these estimations, we determined the saturation intensity values, which were remarkably low, below approximately 22 mW cm^{-2}. We also calculated the maximum achievable birefringence for each compound. In all cases, the change in the refractive index (Δn) was found to be significantly high, in the range of 10^{-4} to 10^{-3}. This combination of high birefringence and low saturation intensity highlights the strong potential of these materials for use in low-power-consumption optical devices. Furthermore, the evaluation of saturation intensity and maximum birefringence provides a more meaningful assessment of the materials' utility in photoswitching applications than the standard n_2 parameter alone.

The dynamics of birefringence changes during growth and decay observed in our materials exhibit a complex, triple-exponential behavior, which is relatively uncommon in the literature. In the studied compounds, the birefringence build-up process can be characterized by fast time constants ranging from 0.28 to 1.20 s, depending on the specific compound (see Fig. 6(b) and Table S6). The intermediate components vary from 4.91 to 18.8 s, while the slowest processes extend to tens or even hundreds of seconds. As expected, the fastest components generally contribute the largest amplitude to the overall birefringence, whereas the slowest components have the smallest contributions. These findings confirm the ability of the materials to modulate optical signals effectively; however, the presence of slower processes suggests the involvement of additional mechanisms in birefringence formation. These may include thermal effects, photo-fluidization, or depth-dependent absorption saturation, all of which require further investigation and fall beyond the scope of this work. Regarding birefringence decay, as previously mentioned, the systems do not fully revert to their initial states after the removal of the excitation light (see Fig. 6(a), Fig. S24 and Table 4), indicating a residual birefringence or the so-called "memory effect". This behavior implies potential applicability in optical data storage. To further quantify this effect, we introduced an additional parameter, ξ (see Table 4), which represents the percentage contribution of the non-reversible birefringence component (Δn_0) to the total induced birefringence (Δn). Notably, all compounds demonstrated a measurable memory effect, with the highest ξ value ($\sim$25%) observed for compound **1c** and the lowest ($\sim$8%) for **1d**. These results suggest that the materials studied here could serve as multifunctional platforms: depending on the thresholding criteria, they could function either as optical memory elements or as reversible optical modulators. The abovementioned combination of fast transition (and even saturation under the low value of power pump intensities) and relatively low recovery with the material's high and constant birefringence are desired properties in development, for instance, in telecommunication devices[46] or modulators.[41]

Conclusions

A new family of TCF-based D–π–A molecules were synthesized *via* simple, cost-effective, and efficient synthetic routes. This series of compounds demonstrates a range of advantageous optical properties, including strong solid-state photoluminescence and efficient photoswitching capabilities. The electronic structures and the ability to form distinct, stable conformers were further supported by quantum chemical calculations. All synthesized compounds exhibited photoisomerization, characterized by well-defined isosbestic points and reversible switching behavior. Importantly, by tuning the number and positional arrangement of –OBn substituents in the donor segment of the molecules, we were able to modulate their photosensitivity, particularly in relation to steric hindrance, which plays a significant role in slowing the thermal relaxation to the more stable isomer. Efficient photoisomerization and photoswitching were observed in both liquid and polymeric systems at remarkably low pumping intensities, comparable to natural sunlight ($\sim$100 mW cm^{-2}[47]), making these materials highly promising for applications requiring low-power operation and moderate switching speeds. Notably, all compounds demonstrated a measurable "memory effect", further underscoring their versatility.

Author contributions

K. L.: investigation, conceptualization, methodology, data curation, formal analysis, verification, visualization, writing – original draft, and writing – review and editing; K. E. S.: conceptualization, resources, methodology, validation and writing – review and editing; K. P.: resources and methodology; R. G.: conceptualization, resources, methodology, validation and writing – review and editing; P. F.: resources, methodology, formal analysis and investigation, validation and writing – review and editing; Y. B.: conceptualization, resources, and writing – review and editing; C. A.: conceptualization, resources, and writing – review and editing; L. S.: conceptualization, methodology, formal analysis, data curation, visualization, writing – original draft, supervision, funding acquisition, and project administration.

Conflicts of interest

There are no conflicts to declare.

Data availability

The data supporting this article have been included as part of the SI with more comprehensive information to facilitate a deeper understanding of the study's findings. The SI contains the methodology, characterization of the synthesized compounds, and their general synthesis along with the results mentioned in the main text. See DOI: **https://doi.org/10.1039/d5tc02366a**.

Acknowledgements

K. L. and L. S. would like to thank the National Science Centre of Poland for financial support within grant no. 2020/39/O/ST5/

0185. K. L. would like to thank the Polish National Agency for Academic Exchange for the financial support provided through internship no. BPN/PRE/2022/1/00028. Calculations have been carried out at the Wroclaw Centre for Networking and Supercomputing. The time-resolved spectrofluorometer used in this work has been funded by the National Laboratory for Photonics and Quantum Technologies, project number POIR.04.02.00.00-B003/18.

References

1 A. Abu-Rayyan, I. Ahmad, N. H. Bahtiti, T. Muhmood, S. Bondock and M. Abohashrh, *et al.*, Recent Progress in the Development of Organic Chemosensors for Formaldehyde Detection, *ACS Omega*, 2023, **8**(17), 14859–14872.

2 Y. Watanabe, H. Sasabe, D. Yokoyama, T. Beppu and H. Katagiri, Kido J. Synthesis, properties, and OLED characteristics of 2,2′-bipyridine-based electron-transport materials: The synergistic effect of molecular shape anisotropy and a weak hydrogen-bonding network on molecular orientation, *J. Mater. Chem. C*, 2016, **4**(17), 3699–3704.

3 Q. Qiu, S. Yang, M. A. Gerkman, H. Fu, I. Aprahamian and G. G. D. Han, Photon Energy Storage in Strained Cyclic Hydrazones: Emerging Molecular Solar Thermal Energy Storage Compounds, *J. Am. Chem. Soc.*, 2022, **144**(28), 12627–12631.

4 I. Bala, J. T. Plank, B. Balamut, D. Henry, A. R. Lippert and I. Aprahamian, Multi-stage and multi-colour liquid crystal reflections using a chiral triptycene photoswitchable dopant, *Nat. Chem.*, 2024, **16**(12), 2084–2090.

5 D. Wang, J. Chen, Y. Wang, X. Hao, H. Peng and Y. Liao, *et al.*, Photoswitching in a Liquid Crystalline Pt(II) Coordination Complex, *Chem. – Eur. J.*, 2024, **30**(20), e202304366.

6 A. M. Rice, C. R. Martin, V. A. Galitskiy, A. A. Berseneva, G. A. Leith and N. B. Shustova, Photophysics Modulation in Photoswitchable Metal–Organic Frameworks, *Chemical Reviews*, American Chemical Society, 2020, pp. 8790–813, vol. 120.

7 M. Mostaghimi, H. Pacheco Hernandez, Y. Jiang, W. Wenzel, L. Heinke and M. Kozlowska, On–off conduction photoswitching in modelled spiropyran-based metal–organic frameworks, *Commun. Chem.*, 2023, **6**(1), 275.

8 C. Hillel, S. Rough, C. J. Barrett, W. J. Pietro and O. Mermut, A cautionary tale of basic azo photoswitching in dichloromethane finally explained, *Commun. Chem.*, 2024, **7**(1), 250.

9 F. Xu, J. Sheng, C. N. Stindt, S. Crespi, W. Danowski and M. F. Hilbers, *et al.*, All-visible-light-driven stiff-stilbene photoswitches, *Chem. Sci.*, 2024, **15**(18), 6763–6769.

10 S. Redon, G. Eucat, M. Ipuy, E. Jeanneau, I. Gautier-Luneau and A. Ibanez, *et al.*, Tuning the solid-state emission of small push-pull dipolar dyes to the far-red through variation of the electron-acceptor group, *Dyes Pigm.*, 2018, **156**, 116–132.

11 A. Gonzalez, E. S. Kengmana, M. V. Fonseca and G. G. D. Han, Solid-state photoswitching molecules: structural design for isomerization in condensed phase, *Materials Today Advances*, Elsevier Ltd, 2020, vol. 6.

12 J. J. B. van der Tol, T. A. P. Engels, R. Cardinaels, G. Vantomme, E. W. Meijer and F. Eisenreich, Photoswitchable Liquid-to-Solid Transition of Azobenzene-Decorated Polysiloxanes, *Adv. Funct. Mater.*, 2023, **33**(36), 2301246.

13 M. Rémond, Z. Zheng, E. Jeanneau, C. Andraud, Y. Bretonnière and S. Redon, 4,5,5-Trimethyl-2,5-dihydrofuran-Based Electron-Withdrawing Groups for NIR-Emitting Push–Pull Dipolar Fluorophores, *J. Org. Chem.*, 2019, **84**(16), 9965–9974.

14 B. Wüstenberg and N. R. Branda, A photoswitchable donor-π-linker-acceptor system based on a modified hexatriene backbone, *Adv. Mater.*, 2005, **17**(17), 2134–2138.

15 J. M. Park, C. Y. Jung, W. D. Jang and J. Y. Jaung, Effect of donor-π-acceptor structure on photochromism of dithienylethene-based dyes, *Dyes Pigm.*, 2020, **177**, 108315.

16 L. Fang, Z. Lin, Y. Zhang, B. Ye, J. Li and Q. Ran, *et al.*, Robust, Ultrafast and Reversible Photoswitching in Bulk Polymers Enabled by Octupolar Molecule Design, *Angew. Chem., Int. Ed.*, 2024, **63**(16), e202402349.

17 S. L. Walden, P. H. D. Nguyen, H. K. Li, X. Liu, M. T. N. Le and L. Xian Jun, *et al.*, Visible light-induced switching of soft matter materials properties based on thioindigo photoswitches, *Nat. Commun.*, 2023, **14**(1), 8298.

18 A. Goulet-Hanssens, F. Eisenreich and S. Hecht, Enlightening Materials with Photoswitches, *Adv. Mater.*, 2020, **32**(20), 1905966.

19 G. Liu, J. Leng, Q. Zhou, Z. Deng, L. Shi and C. Fan, *et al.*, Fluorescence photoswitch of stiff-stilbene derivatives for anti-counterfeiting, *Dyes Pigm.*, 2022, **203**, 110361, DOI: 10.1016/j.dyepig.2022.110361.

20 V. Trovato, S. Sfameni, G. Rando, G. Rosace, S. Libertino and A. Ferri, *et al.*, A Review of Stimuli-Responsive Smart Materials for Wearable Technology in Healthcare: Retrospective, Perspective, and Prospective, *Molecules*, 2022, **27**, 5709.

21 K. Li, Y. Xiang, X. Wang, J. Li, R. Hu and A. Tong, *et al.*, Reversible photochromic system based on rhodamine B salicylaldehyde hydrazone metal complex, *J. Am. Chem. Soc.*, 2014, **136**(4), 1643–1649.

22 L. Hu, Q. Zhang, X. Li and M. J. Serpe, Stimuli-responsive polymers for sensing and actuation, *Materials Horizons*, Royal Society of Chemistry, 2019, pp. 1774–93, vol. 6.

23 S. Shruthi, M. Smahel, M. Kohout, G. Shanker and G. Hegde, Influence of linking units on the photo responsive studies of azobenzene liquid Crystals: Application in optical storage devices, *J. Mol. Liq.*, 2021, **339**, 116744, DOI: 10.1016/j.molliq.2021.116744.

24 J. Hu, T. Han, Y. Liu, X. Zhang, Y. Duan and Z. Li, *et al.*, Strategy for optical data encryption and decryption using a D-A type stimuli-responsive AIE material, *Spectrochim. Acta, Part A*, 2020, 239.

25 T. Ganguly, P. Pal, A. Paul and S. Baitalik, Synthesis and manifold but controllable emission switching of stilbene-appended polyaromatic terpyridine derivatives *via* aggregation and *trans–cis* isomerization, *J. Photochem. Photobiol., A*, 2022, **430**, 113966, DOI: 10.1016/j.jphotochem.2022.113966.

26 U. Endesfelder, S. Malkusch, B. Flottmann, J. Mondry, P. Liguzinski and P. J. Verveer, *et al.*, Chemically induced photoswitching of fluorescent probes-A general concept for super-resolution microscopy, *Molecules*, 2011, **16**(4), 3106–3118.

27 M. Ipuy, Y. Y. Liao, E. Jeanneau, P. L. Baldeck, Y. Bretonnière and C. Andraud, Solid state red biphotonic excited emission from small dipolar fluorophores, *J. Mater. Chem. C*, 2015, **4**(4), 766–779.

28 D. J. Stewart, M. J. Dalton, S. L. Long, R. Kannan, Z. Yu and T. M. Cooper, *et al.*, Steric hindrance inhibits excited-state relaxation and lowers the extent of intramolecular charge transfer in two-photon absorbing dyes, *Phys. Chem. Chem. Phys.*, 2016, **18**(7), 5587–5596.

29 Z. C. Yang, M. Wang, A. M. Yong, S. Y. Wong, X. H. Zhang and H. Tan, *et al.*, Intrinsically fluorescent carbon dots with tunable emission derived from hydrothermal treatment of glucose in the presence of monopotassium phosphate, *Chem. Commun.*, 2011, **47**(42), 11615–11617.

30 T. Han, X. Gu, J. W. Y. Lam, A. C. S. Leung, R. T. K. Kwok and T. Han, *et al.*, Diaminomaleonitrile-based Schiff bases: aggregation-enhanced emission, red fluorescence, mechanochromism and bioimaging applications, *J. Mater. Chem. C*, 2016, **4**(44), 10430–10434.

31 J. Chen, D. Li, W. Chi, G. Liu, S. H. Liu and X. Liu, *et al.*, A Highly Reversible Mechanochromic Difluorobenzothiadiazole Dye with Near-Infrared Emission, *Chem. – Eur. J.*, 2018, **24**(15), 3671–3676.

32 S. Dhar, D. K. Rana, S. Singha Roy, S. Roy, S. Bhattacharya and S. C. Bhattacharya, Effect of solvent environment on the Photophysics of a newly synthesized bioactive 7-oxy(5-selenocyanato-pentyl)-2*H*-1-benzopyran-2-one, *J. Lumin.*, 2012, **132**(4), 957–964.

33 C. Bannwarth, S. Ehlert and S. Grimme, GFN2-xTB – An Accurate and Broadly Parametrized Self-Consistent Tight-Binding Quantum Chemical Method with Multipole Electrostatics and Density-Dependent Dispersion Contributions, *J. Chem. Theory Comput.*, 2019, **15**(3), 1652–1671.

34 M. J. Frisch; G. W. Trucks; H. B. Schlegel; G. E. Scuseria; M. A. Robb; J. R. Cheeseman; G. Scalmani; V. Barone; G. A. Petersson; H. Nakatsuji; X. Li; M. Caricato; A. V. Marenich; J. Bloino; B. G. Janesko; R. Gomperts; B. Mennucci and Hratch, *Gaussian 16, Revision C.01*, 2016.

35 T. Shiozaki, BAGEL: Brilliantly Advanced General Electronic-structure Library, *Wiley Interdiscip. Rev.: Comput. Mol. Sci.*, 2018, **8**(1), e1331.

36 F. Neese, F. Wennmohs, U. Becker and C. Riplinger, The ORCA quantum chemistry program package, *J. Chem. Phys.*, 2020, **152**(22), 224108.

37 B. De Souza, F. Neese and R. Izsák, On the theoretical prediction of fluorescence rates from first principles using the path integral approach, *J. Chem. Phys.*, 2018, **148**(3), 035204.

38 A. Airinei, N. Fifere, M. Homocianu, C. Gaina, V. Gaina and B. C. Simionescu, Optical properties of some new azo photoisomerizable bismaleimide derivatives, *Int. J. Mol. Sci.*, 2011, **12**(9), 6176–6193.

39 A. Natansohn and P. Rochon, Photoinduced motions in azo-containing polymers, *Chem. Rev.*, 2002, **102**(11), 4139–4175.

40 A. Szukalski, K. Haupa, A. Miniewicz and J. Mysliwiec, Photoinduced birefringence in PMMA polymer doped with photoisomerizable pyrazoline derivative, *J. Phys. Chem. C*, 2015, **119**(18), 10007–10014.

41 A. Szukalski, R. Stottko, P. Krawczyk, B. Sahraoui and B. Jędrzejewska, Application of the pyrazolone derivatives as effective modulators in the opto-electronic networks, *J. Photochem. Photobiol., A*, 2023, **437**, 114482.

42 L. M. Silva, D. L. Silva, M. V. Boas, Y. Bretonniere, C. Andraud and M. G. Vivas, Probing the high performance of photoinduced birefringence in V-shaped azo/PMMA guest–host films, *RSC Adv.*, 2020, **10**(67), 40806–40814.

43 F. Fan, Y. Liu, Y. Hong, J. Zang, A. Wu and T. Zhao, *et al.*, Improving the polarization-holography performance of PQ/PMMA photopolymer by doping with THMFA, *Opt. Express*, 2018, **26**(14), 17794.

44 C. R. Mendonça, L. Misoguti, A. A. Andrade, S. B. Yamaki, V. D. Dias and T. D. Z. Atvars, *et al.*, Photoinduced birefringence in di-azo compounds in polystyrene and poly(methyl methacrylate) guest-host systems, *Opt. Mater.*, 2007, **30**(2), 216–221.

45 B. N. Sunil, W. S. Yam and G. Hegde, Photoresponsive behavior of hydrophilic/hydrophobic-based novel azobenzene mesogens: Synthesis, characterization and their application in optical storage devices, *RSC Adv.*, 2019, **9**(69), 40588–40606.

46 P. Drexler and P. Fial, Optical Fiber Birefringence Effects – Sources, Utilization and Methods of Suppression. Recent Progress in Optical Fiber, *Recent Progress in Optical Fiber Research*, 2012, pp. 127–150.

47 D. R. Myers, Solar radiation modeling and measurements for renewable energy applications: Data and model quality, *Energy*, 2005, **30**(9), 1517–1531.

